





# Molecular probes for tracking lipid droplet membrane dynamics

Received: 15 February 2024

Accepted: 16 October 2024

Published online: 31 October 2024

 Check for updates

Lingxiu Kong<sup>1,11</sup>, Qingjie Bai<sup>1,2,11</sup>, Cuicui Li<sup>3,4,5,6,11</sup>, Qiqin Wang<sup>1,7,11</sup>, Yanfeng Wang<sup>1</sup>, Xintian Shao<sup>1,2,8</sup>, Yongchun Wei<sup>1</sup>, Jiarao Sun<sup>1</sup>, Zhenjie Yu<sup>1</sup>, Junling Yin<sup>2</sup>, Bin Shi<sup>2,8</sup>, Hongbao Fang<sup>9</sup>, Xiaoyuan Chen<sup>10</sup> <sup>3,4,5,6,10</sup>  & Qixin Chen<sup>1,2,3,5,6,10</sup>  

Lipid droplets (LDs) feature a unique monolayer lipid membrane that has not been extensively studied due to the lack of suitable molecular probes that are able to distinguish this membrane from the LD lipid core. In this work, we present a three-pronged molecular probe design strategy that combines lipophilicity-based organelle targeting with microenvironment-dependent activation and design an LD membrane labeling pro-probe called **LDM**. Upon activation by the HClO/CIO<sup>-</sup> microenvironment that surrounds LDs, **LDM** pro-probe releases **LDM-OH** probe that binds to LD membrane proteins thus enabling visualization of the ring-like LD membrane. By utilizing **LDM**, we identify the dynamic mechanism of LD membrane contacts and their protein accumulation parameters. Taken together, **LDM** represents the first molecular probe for imaging LD membranes in live cells to the best of our knowledge, and represents an attractive tool for further investigations into the specific regulatory mechanisms with LD-related metabolism diseases and drug screening.


Lipid droplets (LDs) are ubiquitous organelles that function as intracellular storage compartments for neutral lipids, primarily triacylglycerols and sterol esters. LD play important roles in lipid metabolism and fatty acid (FA) synthesis, and regulate many aspects of energy homeostasis and cell growth<sup>1</sup>. Structurally, LD consists of a neutral lipid core surrounded by a phospholipid monolayer that serves as the membrane<sup>2</sup>. Recent studies have revealed that LD function is orchestrated by a number of proteins that act as gatekeepers by receiving external signals and regulating LD internal metabolism, contact with

other organelles, and cargo exchange<sup>3,4</sup>. These proteins form stable associations with the phospholipid monolayer either through embedding or adherence, and are essential for controlling LD membrane dynamics. Although recognized to be of critical importance, and influenced by factors such as cell type, environmental conditions, and metabolic states<sup>5</sup>, LD membrane dynamics remains poorly understood in terms of specific regulatory mechanisms and biological functions<sup>6</sup>. This is primarily due to the lack of molecular tools that can be used for focused studies of the LD membrane.

<sup>1</sup>School of Pharmaceutical Sciences, Shandong First Medical University & Shandong Academy of Medical Sciences, Jinan, Shandong 250117, PR China.

<sup>2</sup>Medical Science and Technology Innovation Center, Shandong First Medical University & Shandong Academy of Medical Sciences, Jinan, Shandong 250117, PR China. <sup>3</sup>Departments of Diagnostic Radiology, Surgery, Chemical and Biomolecular Engineering, and Biomedical Engineering, Yong Loo Lin School of Medicine and College of Design and Engineering, National University of Singapore, Singapore 119074, Singapore. <sup>4</sup>Clinical Imaging Research Centre, Centre for Translational Medicine, Yong Loo Lin School of Medicine, National University of Singapore, Singapore 117599, Singapore. <sup>5</sup>Nanomedicine Translational Research Program, Yong Loo Lin School of Medicine, National University of Singapore, Singapore 117597, Singapore. <sup>6</sup>Theranostics Center of Excellence (TCE), Yong Loo Lin School of Medicine, National University of Singapore, 11 Biopolis Way, Helios, Singapore 138667, Singapore. <sup>7</sup>College of Pharmacy, Jinan University, Guangzhou 510632, PR China. <sup>8</sup>Neck-Shoulder and Lumbocruclal Pain Hospital, Shandong First Medical University & Shandong Academy of Medical Sciences, Jinan, Shandong 250117, PR China. <sup>9</sup>College of Chemistry and Materials Science, Nanjing Normal University, Nanjing 210023, PR China.

<sup>10</sup>Institute of Molecular and Cell Biology, Agency for Science, Technology, and Research (A\*STAR), 61 Biopolis Drive, Proteos, Singapore 138673, Singapore.

<sup>11</sup>These authors contributed equally: Lingxiu Kong, Qingjie Bai, Cuicui Li, Qiqin Wang.  e-mail: [chen.shawn@nus.edu.sg](mailto:chen.shawn@nus.edu.sg); [chenqixin@sdfmu.edu.cn](mailto:chenqixin@sdfmu.edu.cn)

Fluorescent molecular probes are widely used tools for labeling subcellular organelles and structures, including LDs. Currently, tens, if not hundreds, of small molecule LD-targeting fluorescent molecular probes have been described in the literature<sup>7</sup>, and used successfully to reveal insights into biophysics, cell biology, metabolism and physiology of LD. Recent notable additions to this toolkit include polarity probes<sup>8,9</sup>, viscosity probes<sup>10</sup>, and LD HClO/CIO<sup>-</sup> microenvironment-responsive probes<sup>11</sup>. However, all these currently available tools have been developed to visualize the neutral lipid core, and not the LD membrane, therefore limiting the insights into this unique subcellular membrane structure and its function and dynamics. Moreover, although fluorescently tagged LD-associated proteins have been used to study processes at the LD membrane, these strategies require the use of genetic manipulation, overexpression, and/or cell fixation. This may limit physiological relevance of the findings and, in the context of cell fixation requirement, prevent live cell imaging.

To overcome these limitations, we propose a three-pronged chemical labeling strategy that selectively labels LD membranes. This strategy integrates lipid-enhanced response, microenvironment activation, and electrostatic interactions present at and around the LD membrane. Thus, we designed a LD membrane (**LDM**) pro-probe (nomenclature analogous to pro-drug terminology) that is specifically delivered to the vicinity of LD membranes based on its physico-chemical properties. We showed that **LDM** is activated by the HClO/CIO<sup>-</sup> found in the LD microenvironment to generate **LDM-OH** probe. **LDM-OH** was subsequently observed to bind to LD membrane-associated proteins through electrostatic interactions, thus selectively visualizing the LD membrane (Fig. 1). By employing **LDM**, we shed light on the LD membrane protein accumulation in live cells, confirming dynamic mechanism of LD membrane contacts with mitochondria and their protein accumulation parameters. Furthermore, we investigated the protein accumulation parameters at the membrane contact, and this relationship is related to the membrane protein per unit area. Taken together, **LDM** overcomes the limitations of current LD membrane labeling techniques, and enables real-time investigation of LD membrane dynamics under physiological conditions.

## Results

### LD membrane-specific fluorescent molecular probe concept and design components

To develop a fluorescent molecular probe suitable for selective visualization of the LD membrane, we employed a three-pronged probe design strategy that uses: (1) lipophilicity to maximize localization in the less polar regions of LD within cells<sup>12</sup>, thus delivering the probe to its subcellular target; (2) microenvironment responsive activation trigger that takes advantage of the fact that LD microenvironment exhibits a localized increase of HClO/CIO<sup>-</sup> levels<sup>11</sup> to transform the pro-probe into (3) a probe capable of electrostatic anchoring with LD membrane proteins (see Fig. 1 for overview of the design strategy). To ensure low polarity and take advantage of the principles of similar solubility<sup>13-15</sup>, we selected (E)-2-(3-(4-hydroxystyryl)-5,5-dimethylcyclohex-2-en-1-ylidene) malononitrile as the starting point for the **LDM** pro-probe due to its low polarity and good fluorescence properties under neutral/weakly alkaline conditions within LDs, effectively eliminating interference from other regions. The **LDM** pro-probe also incorporated the N, N-dimethylthiocarbamate group as the HClO/CIO<sup>-</sup> responsive element, as it reacts with HClO/CIO<sup>-</sup> found in the LD microenvironment<sup>11</sup> to expose the phenolic hydroxyl group in **LDM-OH**. The phenolic -OH in **LDM-OH** can form electrostatic interactions with amino groups in LD membrane proteins, similarly to what is seen in drug design<sup>16,17</sup>, thus effectively labeling the LD membrane. Additionally, the HClO/CIO<sup>-</sup>-triggered reaction transforms the green fluorescent pro-probe **LDM** to a red fluorescent **LDM-OH**, allowing for accurate visualization (Fig. 1). Taken together, our pro-probe design of

**LDM** (green color) ensures directed delivery to LD based on lipophilicity of the molecule, rapid response to the LD microenvironment (HClO/CIO<sup>-</sup>) through formation of the red fluorescent **LDM-OH**, that subsequently binds LD membrane proteins, completing the labeling process of the LD membranes. Below, we describe results of detailed characterization and validation of **LDM** and **LDM-OH**, and illustrate its use for imaging LD membrane in live cells.

### Optical selectively, physical properties characterization of **LDM** in vitro

We synthesized the pro-probe molecule through a *Knoevenagel* condensation reaction<sup>18</sup> (Supplementary Fig. 1-2) and confirmed the structure by standard methods (Supplementary Fig. 3-11). To confirm that HClO/CIO<sup>-</sup> triggers activation of **LDM**, we added NaClO (HClO/CIO<sup>-</sup> donor<sup>19</sup>), which led to an increase in fluorescence intensity at 561 nm, showing a linear correlation with  $R^2 = 0.98933$ , and a detection limit of 6.8  $\mu$ M (Fig. 2a-c, Supplementary Fig. 13), which depends on the environment of in vitro simulation testing<sup>20-22</sup>. The **LDM** to CIO<sup>-</sup> reaction was completed in 40 min (Supplementary Fig. 14), with a fluorescence quantum yield of 0.37 (Supplementary Fig. 15). Additionally, we observed a decrease in absorption peak at 405 nm, suggesting that **LDM** responds to HClO/CIO<sup>-</sup> to generate **LDM-OH** in vitro. (Supplementary Fig. 16). We further verified that the product was indeed **LDM-OH** using high-resolution mass spectrometry (Supplementary Fig. 12). Simultaneously investigated the effects of viscosity and polarity on **LDM** and **LDM-OH**. Results indicate that an increase in viscosity has a non-linear strengthening effect on the fluorescence intensity of **LDM** and **LDM-OH**. The effect of polarity on **LDM** is not significant. When the content of dioxane is 40%-50%, the polarity of the solution enhances the fluorescence intensity of **LDM-OH** (Supplementary Fig. 17). Since the probe **LDM** labels the LDs membrane imaging rather than the contents, according to our experimental results (Fig. 3a and Fig. 4e), there was no significant difference in the lipid droplet membrane imaging between the normal and drug-induced treatment groups.

To demonstrate **LDM**'s selectivity towards HClO/CIO<sup>-</sup>, various reactive oxygen species and nitrogen species were tested. At 10.0  $\mu$ M, only HClO/CIO<sup>-</sup> triggered a fluorescence signal response centered at 665 nm, while no significant changes were observed in the presence of other ROS or biologically related species, such as H<sub>2</sub>O<sub>2</sub>, ·OH, ·O<sub>2</sub><sup>-</sup>, metal ions (Fig. 2e, Supplementary Figs. 18, 19), or pH changes (Fig. 2d). These results indicate that **LDM** is selectively responsive to HClO/CIO<sup>-</sup>.

To confirm that **LDM** is able to localize to lipid-rich regions, we conducted a lipophilicity experiment<sup>23</sup> to assess the probe's distribution in phosphate buffer. We dissolved **LDM** in the phosphate buffer and mixed the buffer with a lipid layer (Fig. 2f). After 10 min, a substantial amount of **LDM** molecules dissolved in the lipids, causing the phosphate buffer to change from yellow to colorless, while the lipid layer transformed from white to yellow. This highlights that **LDM** has the capacity to distribute into the lipid environment, suggesting its ability to target LD.

To investigate whether **LDM-OH** is able to form electrostatic interactions with LD membrane proteins, we selected seven representative LD membrane proteins<sup>24-27</sup> and performed docking assays with **LDM-OH** (Fig. 2g, for details, see Supplementary Fig. 20). These assays confirmed the strong binding of **LDM-OH** to the membrane proteins. Furthermore, we employed an SDS-PAGE gel electrophoresis experiment to validate **LDM-OH**'s effective binding to the entire protein in the cell, resulting in fluorescent labeling of the proteins (Fig. 2h). This result substantiates that the phenolic hydroxyl group of **LDM-OH** can serve to anchor the probe to LD membrane proteins.

Collectively, the results of our in vitro and docking studies provide strong support for **LDM** as the LD-localizing pro-probe that's activated by HClO/CIO<sup>-</sup> into **LDM-OH** probe that labels LD membrane proteins to enable selective imaging of LD membranes.

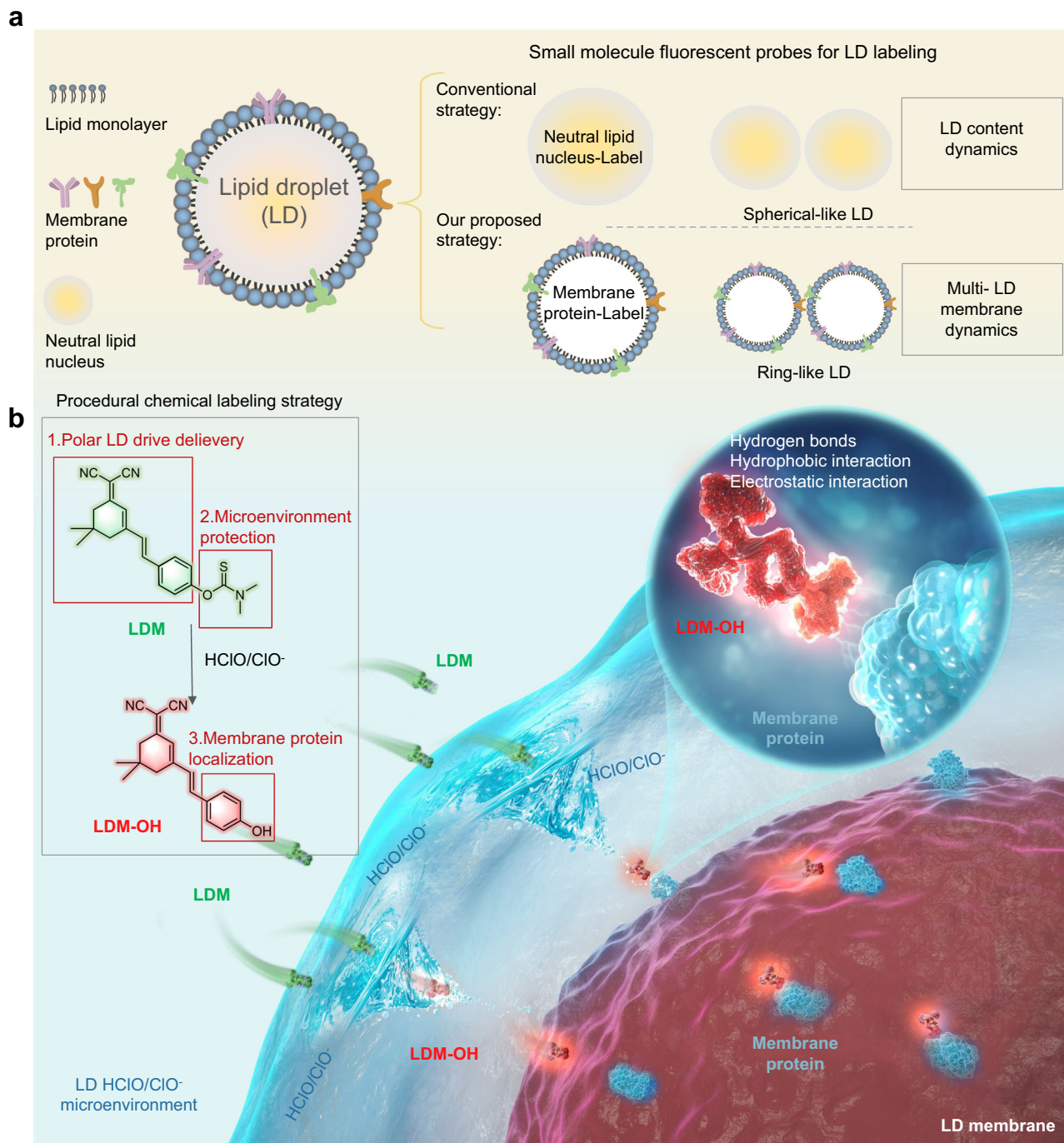


**Fig. 1 | Schematic diagram of chemical strategy to selectively label LD membranes. a** Schematic diagram of the LD chemical labeling strategy. Traditionally, LD labeling strategies using small molecule fluorescent probes mainly focused on labeling neutral lipid nuclei, resulting in spherical-like LD to check the dynamics of content. To achieve a dynamic description of multi-LD membrane dynamics, we propose a approach that involves labeling membrane proteins with a small molecule fluorescent probe, specifically yielding ring-like LD structures. **b** Schematic diagram of the chemical probe labeling mechanism for LD membrane structure.

The three-pronged molecular probe design strategy employs a pro-probe called **LDM**, which combines lipid enhanced response, microenvironment activation, and electrostatic interaction. This comprehensive approach enables the specific delivery of **LDM** to the vicinity of LD membranes. Upon activation by the HClO/CIO<sup>-</sup> microenvironment, **LDM-OH** becomes exposed and binds to LD membranes through electrostatic interaction, facilitating labeling of LD membrane structure. Image created with Photoshop and Microsoft PowerPoint.

### Characterization of LDM in live cells

We first evaluated the cytotoxicity of LDM and LDM-OH on HeLa/HepG2 cell lines and found that the toxic effect of LDM on cell activity was negligible (Supplementary Figs. 21–22). Additionally, we established that LDM entered cells via an energy-dependent mechanism (Supplementary Figs. 23–25). In recent years, multiple excellent studies have been reported in the field of LD fusion<sup>28</sup>, fission<sup>29</sup>, cytosolic

and nuclear LDs movement<sup>30</sup>, and the interaction between organelles<sup>31</sup>. Using structured illumination microscopy (SIM)<sup>32,33</sup>, we captured LDM-stained cells under SIM-488 laser (LDM<sup>488</sup>) and SIM-561 laser (LDM<sup>561</sup>) (Fig. 3a). We observed the presence of green fluorescent particles of random sizes (Zoom 1#, Fig. 3a) and a regular, red fluorescent ring-like structure (Zoom 1#, Fig. 3a). To further characterize the ring-like structure, we constructed a 3D-surface fluorescent map

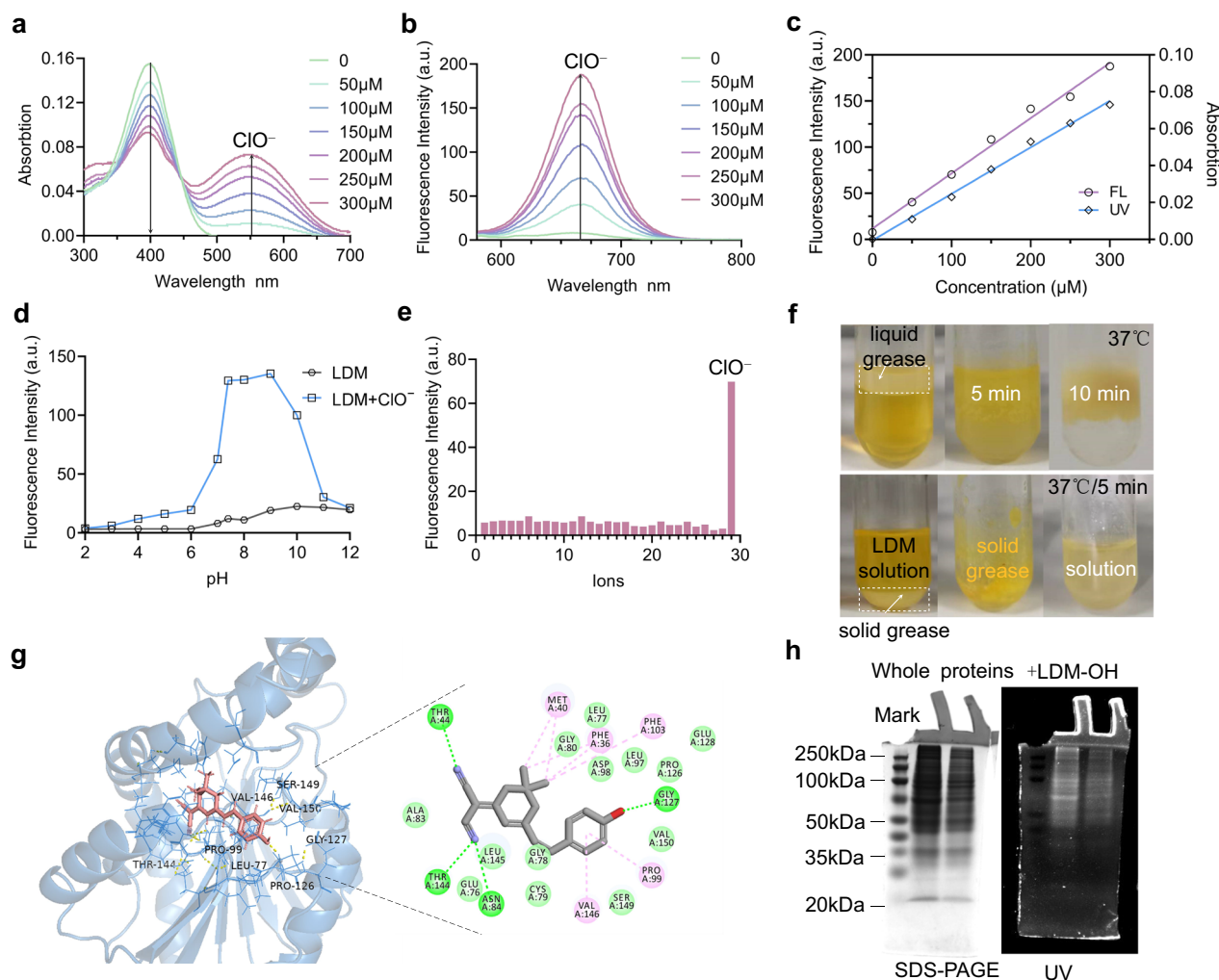


**Fig. 2 | Optical selectivity, physical properties characterization of LDM in vitro.**

**a, b** The absorption and fluorescence spectra of **LDM** (10.0  $\mu\text{M}$ ) in different  $\text{NaClO}$  (0–300.0  $\mu\text{M}$ ) solution (DMSO-PBS, 1:99, v/v, pH = 7.4),  $\lambda_{\text{ex}}$  = 561 nm, slit: 5 nm/5 nm/700 V. **c** Linear relationship between UV absorption and fluorescence intensity and  $\text{HClO}/\text{ClO}^-$  concentration in **a** and **b**, the linear regression equation is determined as  $Y = 59658.07143X + 11.58132$ , with a linear correlation  $R^2 = 0.98933$ , where  $X$  represents the concentration of  $\text{ClO}^-$  and  $Y$  represents the fluorescence intensity of **LDM** at 665 nm (**d**) The fluorescence intensity change of **LDM** (10.0  $\mu\text{M}$ ) in different pH (2–12) solutions with (red) or without (black)  $\text{ClO}^-$  (100  $\mu\text{M}$ ) ( $\lambda_{\text{ex}}$  = 561 nm), **e** The selectivity of **LDM** towards  $\text{ClO}^-$ , and various reactive oxygen species in DMSO-PBS solution (100.0  $\mu\text{M}$ , 1:99, v/v, pH = 7.40). 1. Blank; 2.  $\text{NO}_2^-$ ; 3.  $\text{t-BuOO}^-$ ; 4.  $\text{PO}_4^{3-}$ ; 5.  $\text{OH}^-$ ; 6.  $\text{HPO}_4^{2-}$ ; 7.  $\text{CH}_3\text{COO}^-$ ; 8.  $\text{F}^-$ ; 9.  $\text{Cl}^-$ ; 10.  $\text{Ag}^+$ ; 11.  $\text{Al}^{3+}$ ; 12.  $\text{Ca}^{2+}$ ;

13.  $\text{Cr}^{3+}$ ; 14.  $\text{Co}^{2+}$ ; 15.  $\text{Fe}^{2+}$ ; 16.  $\text{Fe}^{3+}$ ; 17.  $\text{Mn}^{2+}$ ; 18.  $\text{Ni}^{2+}$ ; 19.  $\text{Pb}^{2+}$ ; 20.  $\text{Zn}^{2+}$ ; 21.  $\text{Cu}^{2+}$ ; 22.  $\text{Hg}^{2+}$ ; 23.  $\text{Cd}^{2+}$ ; 24.  $\text{H}_2\text{O}_2$ ; 25.  $\text{NO}$ ; 26.  $\text{SO}_4^{2-}$ ; 27.  $\text{ONOO}^-$ ; 28.  $\text{O}_2$ ; 29.  $\text{ClO}^-$ . **f** Lipophilic assay for testing the distribution of the **LDM** in phosphate buffer. **LDM** molecules dissolved in the lipids, causing the phosphate buffer to change from yellow to colorless, while the lipids transformed from white to yellow, suggest **LDM** with a lipid response behavior. **g** Macromolecular docking of **LDM-OH** and representative lipoprotein (Q6UX53). **h** The whole protein SDS-PAGE electrophoresis (left) and UV image for the protein gel incubation with **LDM-OH** (37  $^\circ\text{C}$ , 2 h) (right), indicating the **LDM-OH** could bind to the whole proteins in HepG2 cells. Three independent biological replicates were performed, and the results were similar. Source data are provided as a source data file.

which demonstrated a uniform distribution of fluorescence within a single ring-like structure (Fig. 3b). The height bimodal fluorescence intensity peaks were found to be equal (Fig. 3c, Supplementary Fig. 26). However, at the contact site with multiple ring-like structures, red fluorescence showed an uneven distribution, resulting in multiple peak shapes of unequal heights (Supplementary Fig. 27). These results suggest that **LDM** reached LDs, underwent chemical transformation to **LDM-OH** and labeled the LD membrane (ring-like structures). The uneven distribution might, therefore, be due to different protein distribution patterns within different red-like ring structures, particularly at the contact site.

To further support that the **Plin2** and **Plin5** proteins<sup>34–36</sup>, known as uniform markers for LD membranes, were used as fluorescent markers for labeling LDs under SIM. Our analysis revealed no significant fluorescence enrichment of **Plin2** or **Plin5** when LD membranes approached each other (Supplementary Fig. 28a, b). To explore the possibility of

specific protein aggregation, we next test **Cidec**<sup>37</sup>, a protein involved in LD fusion, which distributes uniformly on single LD membranes but enriches at membrane contact sites upon LD interactions. Remarkably, our **LDM** probe and labeled LD membranes accurately reflected this **Cidec** aggregation, with significant enrichment at membrane contact sites upon LD membrane proximity (Supplementary Fig. 29a, b). This validates that the fluorescence enhancement observed with **LDM**-labeled LD membranes is not mere fluorescence overlap but an indicator of protein dynamics at membrane contact sites.

Importantly, the size distribution of the red ring-like structures labeled by **LDM**<sup>561</sup> matched the reported LD size range<sup>38</sup>. This suggests that the red ring-like structures labeled by **LDM** using SIM may close to represent the LD membrane (Supplementary Fig. 30). To test this hypothesis, we performed localization experiments using a commercial LD probe that labels the core neutral lipids<sup>39</sup>, **Lipi-B**<sup>405</sup>, and co-incubated cells with **Lipi-B** and **LDM**. As expected, the

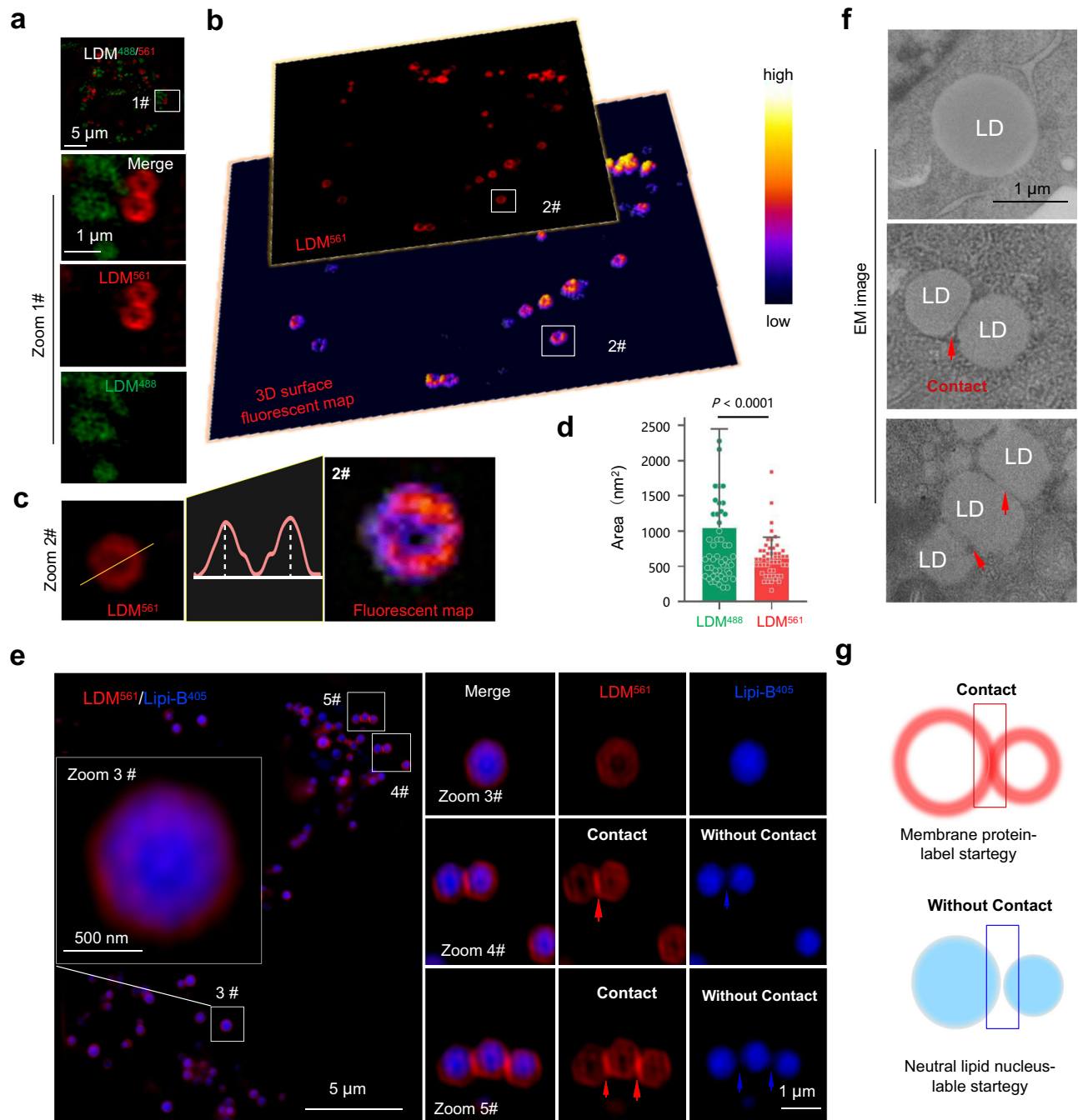


**Fig. 3 | Super-resolution imaging for ring-like LD membrane tracking with LDM pro-probe.** **a** HepG2 cells incubated with 10.0  $\mu\text{M}$  LDM under SIM 488 laser and 561 laser. Zoomed-in images are of white rectangle #1. **b** 3D surface fluorescent map of HepG2 cells incubated with LDM under SIM 561 laser, Zoomed-in images are of white rectangle #2. **c** SIM imaging and 3D surface fluorescent map of representative single particles stained with LDM<sup>561</sup>, yellow dotted line in zoomed-in image #2 indicate region for fluorescence analysis. **d** Quantitative analysis of the area for fluorescent punctate labeled with LDM<sup>488</sup> and LDM<sup>561</sup>. Data are mean  $\pm$  SD ( $n = 50$  areas from 10 cells). **e** SIM images of HepG2 cells co-stained with commercial Lipi-B<sup>405</sup> and LDM<sup>561</sup> channel, Zoomed-in images are of white rectangles #3, #4, #5. Three independent imaging replicates were performed, and the results were

similar. **f** Electron microscopy imaging of single LD and multi-LD contact event. Three independent imaging replicates were performed, and the results were similar. **g** Schematic comparison between membrane protein ring-like LD labeling strategy and content spherical-like LD labeling strategy, suggests the traditional spherical-like labeling strategy cannot well characterize the membrane interaction event of multiple LD. LDM<sup>488</sup> channel:  $\lambda_{\text{ex}} = 488$  nm, Em max 525 nm (500–550 nm); LDM<sup>561</sup> channel:  $\lambda_{\text{ex}} = 561$  nm, Em max 665 nm (600–700 nm); Lipi-B<sup>405</sup> channel:  $\lambda_{\text{ex}} = 405$  nm, Em max 447 nm (417–476 nm). Statistical analysis was performed using two-tailed unpaired Student's *t*-test, and the data were presented as mean  $\pm$  SD.  $P < 0.05$  was considered statistically significant. Source data are provided as a source data file.

LDM<sup>561</sup>-labeled red ring-like structure effectively surrounded the Lipi-B<sup>405</sup>-labeled area indicative of LD core (Fig. 3e, enlargement Zoom 3#–5#, Supplementary Figs. 31–32), confirming that LDM labels the area immediately surrounding the LD core, most likely the LD membrane. However, we also noted that the area labeled by Lipi-

B<sup>405</sup> was somewhat smaller than the ring labeled by LDM<sup>561</sup> (Supplementary Figs. 33–34, which can be explained by the known phenomenon that lipid dyes aggregate in the center of LD<sup>39</sup>). Therefore, we believe that the size of the LDM-based ring under SIM is a more accurate representation of the LD size, compare to traditional

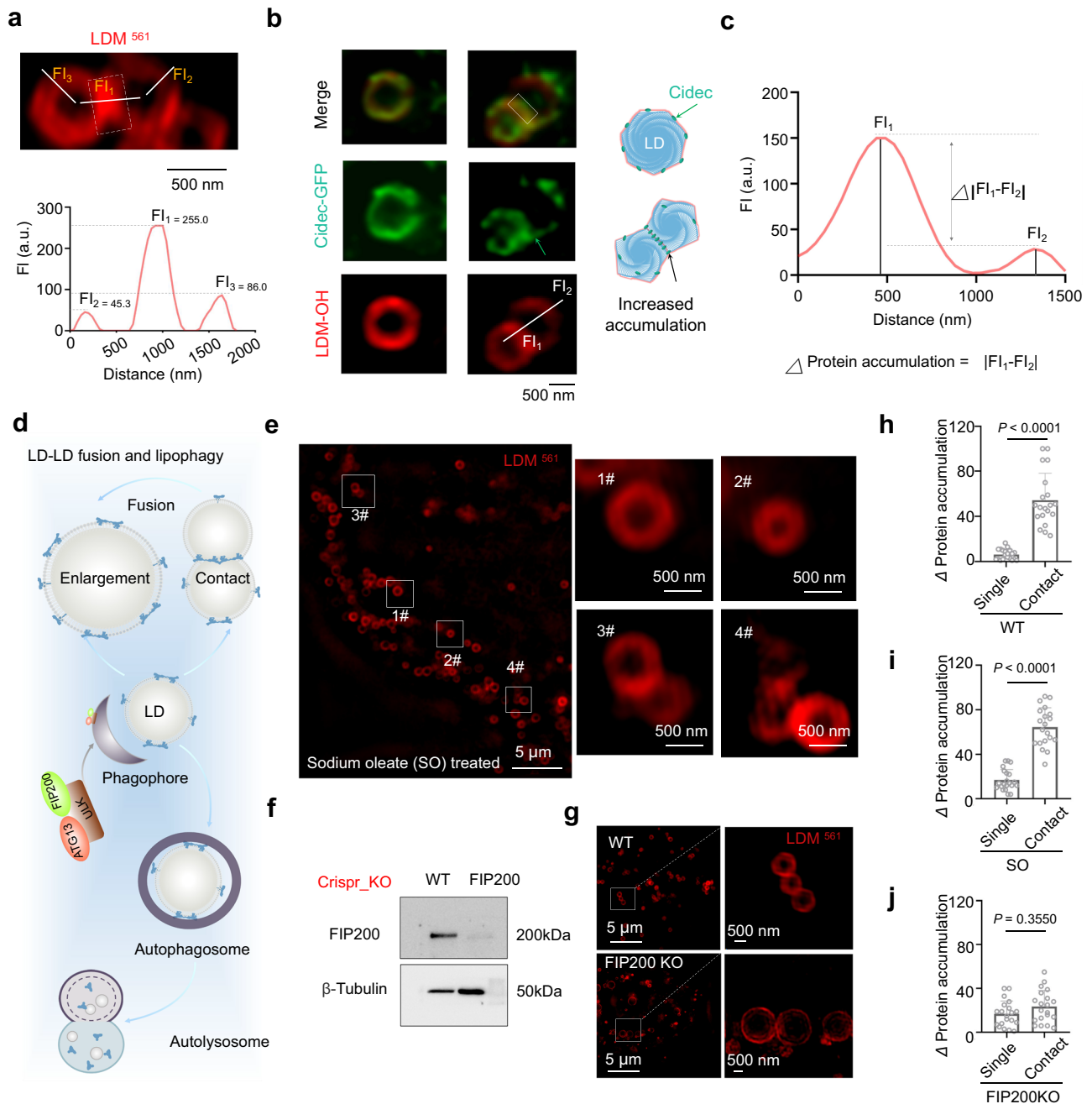


**Fig. 4 | LDM fluorescence aggregation as an indicator of membrane contact protein accumulation parameters.** **a** Representative SIM image of LD membrane dynamic stained with **LDM** and Lipi-B<sup>405</sup>, and simulation for single LD dynamic. **b** Representative SIM image of LD co-stained with Cidec-GFP in **LDM**-561 channel, and the schematic diagram of Cidec-GFP location in LD protein accumulation formation. Image created with Microsoft PowerPoint. **c** According to the **LDM-OH** imaging analysis of **b**, assuming that the protein accumulation is positively correlated with fluorescence intensity,  $\Delta$ protein accumulation =  $|FI_1 - FI_2|$ , the data is obtained through imageJ. **d** Schematic diagram of LD-LD fusion and lipophilicity process, Image created with Microsoft PowerPoint. **e** SIM image of HepG2 cells treated with 100  $\mu$ M sodium oleate, for 24 h and then stained with **LDM**, Zoomed-in images are of white rectangles #1-#4. white dotted line in zoomed-in images #1-#4

indicates the region for fluorescence analysis. **f** Western blot for detecting FIP200 protein expression in HepG2 gene-edited cells. **g** Representative SIM image of LD stained with **LDM** in HepG2 WT cells and FIP200KO cells, Zoomed-in images are of white rectangle. The white dotted line in zoomed-in images #1-#4 indicates the region for fluorescence analysis. **h-j** Quantitative analysis of protein accumulation changes in WT, sodium oleate and FIP200KO HepG2 cells. Data are mean  $\pm$  SD ( $n = 20$  areas from 10 cells). Cidec-GFP channel:  $\lambda_{ex} = 488$  nm,  $\lambda_{em}$  max 525 nm (500-550 nm); **LDM-OH** channel:  $\lambda_{ex} = 561$  nm,  $\lambda_{em}$  max 665 nm (600-700 nm). Three independent imaging or biological replicates were performed, and the results were similar. Statistical analysis was performed using two-tailed unpaired Student's *t*-test, and the data were presented as mean  $\pm$  SD.  $P < 0.05$  was considered statistically significant. Source data are provided as a source data file.

microscopy. Importantly, we observed that unlike Lipi-B that can't visualize the actual physical contact between LD (Fig. 3e, Zoom 4#-5#, Supplementary Fig. 35), the LDM<sup>561</sup>-labeled ring-like LD structure provided valuable information for the multiple LD contacts (Supplementary Fig. 36), consistent with those seen by the electron

microscopy (EM) (Fig. 3f). Consequently, we propose that our probe captures the more precise contact sites between multiple LD interactions in living cells (Fig. 3g, Supplementary Fig. 37), compared to probe labeling technology located in the LD core (Supplementary Fig. 30 and Supplementary Fig. 33). Furthermore, the

**LDM** alone does not trigger the formation of LD membrane contact sites (Supplementary Fig. 38).

### **LDM fluorescence aggregation as an indicator of membrane contact protein accumulation parameters**

It is widely accepted that LD membrane proteins move within the membrane and this mobility plays critical roles in physiological processes within living cells<sup>5</sup>. In agreement with this, we observed that the membrane protein labeled with **LDM**<sup>561</sup> exhibited dynamic fluorescent coverage patterns in the inner shell of a single representative LD (Fig. 4a). We also noticed that the fluorescence intensity of the **LDM**<sup>561</sup> marker at the contact site is more than twice that of the non-contact site (Supplementary Fig. 39), suggesting that the high fluorescence intensity might be due to accumulation of labeled proteins at specific. To verify this hypothesis, we co-labeled an LD membrane-related protein, Cidec-GFP, which is known to mediate adhesion between membranes<sup>37</sup>. Results demonstrated a matching trend between the positioning of Cidec-GFP and the **LDM**-OH-labeled membrane protein in the LD membrane contact area (Fig. 4b, Supplementary Fig. 40), further confirming **LDM**'s capability to accurately report on increased migration and co-localization of membrane proteins in the contact area, as indicated by increased fluorescence intensity at the contact sites (Fig. 4b, green arrow). This result further validates **LDM**'s utility as a marker for protein accumulation between membrane contacts, reveals that protein accumulation may depend on increased co-localization of LD membrane proteins, and provides a tool for evaluating adhesion parameters in diverse cellular processes.

To further quantify protein co-localization between contact sites, we introduced the accumulation parameter, which is the difference between the number of **LDM**-labeled fluorescent protein molecules at the contact site and the diagonal (Fig. 4c). Using this system, we tested the effect of chemical drug/gene intervention on accumulation parameters. Firstly, we stimulated HepG2 cells with sodium oleate for 24 h and observed a significant increase in the number of membrane contacts, including single, multiple, and even linear membrane contacts (Fig. 4e, Supplementary Figs. 41–42). More importantly, the fluorescence intensity of **LDM**-labeled membrane proteins in the membrane contact area increased (Fig. 4h), indicating heightened accumulation as it is generally accepted that the protein accumulation of the membrane is related to the number of proteins per unit area<sup>40</sup>.

To further verify the applicability of our probe to characterize the protein accumulation parameters, we further investigated the relationship between membrane protein accumulation and LD size. Studies have shown that blocking the process of lipophagy can inhibit the degradation of the contents of the LDs and effectively increase the area of the LD membrane. To examine this relationship further, we knocked out (KO) a key autophagy protein FIP200<sup>41</sup> (Fig. 4f–g), thus inhibiting lipophagy to increase the accumulation of lipid components and consequently the volume of LD<sup>42</sup> (Fig. 4d). As anticipated, the size of LD in FIP200KO cells significantly increased (Supplementary Fig. 43), while the fluorescence intensity of the **LDM**-labeled membrane protein in the contact area did not increase significantly, relative to a single LD (Fig. 4j). We also knocked out ATG13, another protein with the key role in autophagy<sup>43</sup>, and observed similar effects (Supplementary Fig. 44). These results indicate that when the unit membrane volume increases, the number of membrane proteins disperses, leading to decreased protein accumulation between the membranes.

In summary, these findings demonstrate that **LDM** fluorescence intensity effectively reflects the accumulation parameters at the membrane contact, and this relationship is related to the membrane protein per unit area.

### **Using LDM to track changes in LD membrane protein accumulation during the period of liver cancer cell starvation**

When tumors progress rapidly, they often enter an energy-deprived state of starvation, necessitating a series of metabolic reprogramming to cope with energy stress<sup>44</sup>. Among them, liver cancer cells will accumulate a large number of LDs in the cells to supply the energy needed during periods of starvation<sup>45,46</sup>. We used **LDM** to measure the changes in the protein accumulation of LD in liver cancer cells, reflecting how these cells utilize LDs during starvation.

We found that the LD in liver cancer cells significantly decrease in a starving state, with the number and area of LD reduced by approximately 2–3 times (Fig. 5a–c) and the triglyceride (TG) content in LDs significantly decreases (Supplementary Fig. 45). Meanwhile, the protein accumulation between LD membranes of cancer cells decreases after starvation, and the number of contact sites between LDs significantly decreases (Fig. 5d–f). The reduction in protein accumulation contact between LDs may be associated with an increase in the utilization of LD during cancer cell starvation. This is consistent with a previous study, which indicates that when cells utilize LD, the contact and fusion between LDs decrease<sup>47</sup>.

Current research suggests that when cells are starved, they utilize LD through LD-mitochondria contact<sup>48</sup>. To examine this, we used **LDM** to investigate the protein accumulation status between LDs and mitochondria. Results showed that under serum-starved conditions, **LDM** accumulates at the contact sites between LD and mitochondrial membrane, while the number of membrane contact sites also increases (Fig. 5g–i). Next, we tested whether the enhanced protein accumulation between LD and mitochondria displayed by **LDM** promotes the utilization of LD by mitochondria. We used mitochondrial ROS (mROS) probe<sup>561</sup> to label mROS, thus indirectly reflecting the amount of energy produced by mitochondria. We found that mROS production increased by about fourfold in cancer cells after starvation (Fig. 5j, k). Meanwhile, we used the FA probe C12<sup>488</sup> to indicate the migration of FAs between LD and mitochondria. The experimental results indicate that after starvation, FAs originally located on LD increase their migration towards mitochondria (Fig. 5l, m, Supplementary Fig. 46). The above results indicate that when liver cancer cells are starving, the protein accumulation between LDs decreases, and the interaction between dispersed LD and mitochondria strengthens. Subsequently, these LDs release FAs, migrate to mitochondria, and are oxidized by mitochondria, thereby providing energy for starving cancer cells (Fig. 5n). In addition to its role in cellular processes, we have explored our tool's potential in drug evaluation. Testing known LD modulators Mos-1<sup>49</sup>, CHE<sup>50</sup>, and tanshinone IIA<sup>51</sup> revealed Mos-1 reduces LD numbers and contact, while CHE increases LD numbers but reduces contact (Supplementary Fig. 47), consistent with prior reports. Notably, our examination of tanshinone IIA with autofluorescence showed it enhances LD numbers, contact, and exhibits a membrane localization labeled by our probe (Supplementary Fig. 48). In summary, we used **LDM** to label LD membranes of liver cancer cells during the period of starvation, drug evaluation, and the drug location. These applications provide an attractive tool for further investigations into the specific regulatory mechanisms and drug discovery associated with LD related metabolism diseases.

## **Discussion**

We successfully developed a fluorescent molecular probe for imaging LD membranes in live cells. Our strategy is based on the use of probe **LDM** that localizes to LD due to its lipophilic properties. Once there, it is activated by the LD microenvironment, more specifically by increased levels of HClO/CIO<sup>-</sup> typically found around LD. This generates the probe, **LDM-OH**, which associates with LD membrane proteins to generate a strong fluorescent signal indicative of the LD membrane. We used this probe to visualize the LD membrane in live

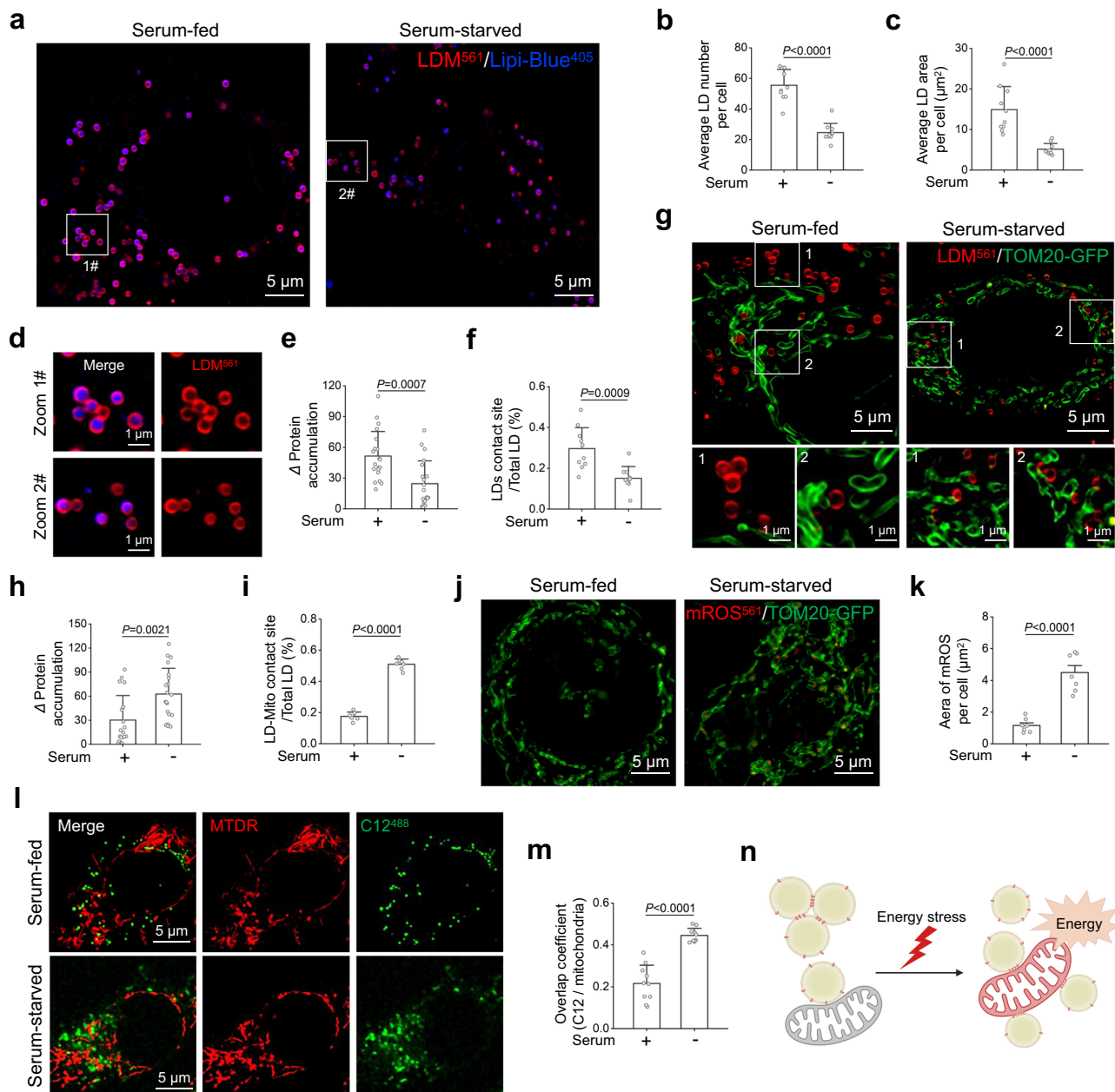


**Fig. 5 | Using LDM to track changes in LD membrane protein accumulation during the period of liver cancer cell starvation.** **a** Representative SIM images of LD changes in HepG2 cells labeled with LDM and Lipi-B<sup>405</sup> under serum-fed and serum-starved. **b, c** Quantitative analysis of the number and area of LD under serum-fed and serum-starved ( $n = 10$  cells). **d** Zoomed-in images are of white rectangle in **a**. Quantitative analysis of intermembrane LD protein accumulation and number of contact sites of LD under serum-fed and serum-starved, **e**  $n = 20$  areas from 10 cells, **f**  $n = 10$  areas from 5 cells. **g** Representative SIM images of LD and mitochondria labeled with LDM and TOM20-GFP under serum-fed and serum-starved. Quantitative analysis of LD and mitochondria protein accumulation and number of contact sites under serum-fed and serum-starved, **h**  $n = 20$  areas from 10 cells, **i**  $n = 7$  areas from 5 cells. **j** Representative SIM images of mitochondrial ROS changes labeled with mROS<sup>561</sup> and TOM20-GFP under serum-fed and serum-starved. **k** Quantitative analysis of FAs and mitochondria under serum-fed and

serum-starved ( $n = 7$  cells). **l** Representative SIM images of FAs and mitochondria in HepG2 cells labeled with C12<sup>488</sup> and MTDR under serum-fed and serum-starved. **m** Quantitative analysis of FAs co-localization with mitochondria under serum-fed and serum-starved ( $n = 10$  cells). **n** Schematic diagram of the process of LD-LD separation and LD-mitochondria interaction after starvation. Created in BioRender. Shao, S. (2024) BioRender.com/e93j405. Lipi-B<sup>405</sup> channel:  $\lambda_{\text{ex}} = 405$  nm,  $\text{Em max}$  447 nm (417–476 nm); LDM-OH channel:  $\lambda_{\text{ex}} = 561$  nm,  $\text{Em max}$  665 nm (600–700 nm); TOM20-GFP channel:  $\lambda_{\text{ex}} = 488$  nm,  $\text{Em max}$  509 nm (505–550 nm); mROS<sup>561</sup> channel:  $\lambda_{\text{ex}} = 561$  nm,  $\text{Em max}$  610 nm (590–610 nm); MTDR channel:  $\lambda_{\text{ex}} = 644$  nm,  $\text{Em max}$  665 nm; C12<sup>488</sup> channel:  $\lambda_{\text{ex}} = 488$  nm,  $\text{Em max}$  510 nm (500–510 nm). Three independent imaging replicates were performed, and the results were similar. Statistical analysis was performed using two-tailed unpaired Student's *t*-test, and the data were presented as mean  $\pm$  SD.  $P < 0.05$  was considered statistically significant. Source data are provided as a source data file.

cells and showed that LDM treatment clearly visualizes the ring-like structure surrounding the neutral lipid core. Furthermore, we could examine LD protein accumulation, both with other LDs and with mitochondria under different conditions. As such, our probe opens new avenues for investigating the specific regulatory mechanisms and

biological functions associated with LD membrane biophysics. Furthermore, our probe overcomes limitations of traditional labeling techniques based on transient fluorescent proteins or immunofluorescence<sup>52</sup>, as it does not require protein overexpression or the use of fixed cells. LDM's ability to selectively label LD membrane



structures and its compatibility with super-resolution microscopy offers a powerful tool for studying LD dynamics in live cells.

Importantly, we established **LDM** as a marker for protein accumulation between LD membrane contacts. By studying the aggregation of fluorescent molecules labeled by **LDM-OH** in the LD membrane contact area, we could accurately measure the changes in LD membrane protein co-localization and evaluate accumulation parameters in various cellular processes. Furthermore, we demonstrated that **LDM** fluorescence aggregation is related to the density of membrane proteins per unit area, shedding light on the relationship between membrane protein accumulation and LD size. The ability of **LDM** to accurately reflect membrane protein accumulation parameters is another important aspect of providing researchers with a powerful tool to investigate the dynamic mechanism of LD membrane contacts, their protein accumulation parameters, and their role in cellular physiology and pathology. By visualizing the aggregation of fluorescent molecules in the LD membrane contact area, **LDM** provides a direct and quantitative measure of membrane protein density, allowing for the investigation of LD-related processes in live cells. This information is critical for understanding cellular physiology and can be applied to study the effects of chemical interventions or genetic modifications on membrane protein accumulation<sup>53</sup>. In the example we use above, **LDM** enabled us to study the effect of starvation on the interface between LDs and mitochondria, demonstrating that liver cancer cells respond to energy stress during hunger by enhancing LD-mitochondria interactions.

More broadly, the versatility of our probe design strategy may yield similar probes for labeling other cellular structures or organelles with distinct membrane properties by tailoring the probe's properties to target specific cellular components. Furthermore, the application of **LDM** in live-cell imaging allows for real-time visualization of LD membrane dynamics under physiological conditions. This capability could be harnessed to study cellular responses to external stimuli, such as changes in nutrient availability or exposure to stressors<sup>54,55</sup>, providing a deeper understanding of cellular adaptation and signaling pathways.

In conclusion, the development of the **LDM** probe represents a significant advancement in the field of chemical biology, enabling selective imaging of LD membrane structures and shedding light on the dynamics and functions of LD in living cells. This approach overcame the limitations of current LD membrane labeling techniques and enabled real-time investigation of LD membrane dynamics under physiological conditions. By applying **LDM**, we gained insights into the biophysical functions of LD membrane dynamics and its relationship with LD protein accumulation parameters, providing valuable information on LD membrane dynamics. Future use of **LDM** holds great potential for advancing our understanding of LD biology and other cellular processes that involve membrane dynamics and protein accumulation.

## Methods

### Synthesis and characterization

For synthesis and characterization of Compound **1**, a solution of isophorone (3.50 mL, 23.50 mmol) and CH<sub>3</sub>COONa (1.60 g, 19.51 mmol) in ethanol (25 mL) was added malononitrile (1.30 g, 20.12 mmol). The reaction was allowed to heat and reflux for 8 h. Purification of crude product by silica gel column chromatography to obtain white powder (2.60 g, 69.01%). Melting point: 70.2–72.6°C; TLC (DCM/PE = 3:1, V/V): R<sub>f</sub> = 0.23; <sup>1</sup>H NMR (400 MHz, CDCl<sub>3</sub>) δ 6.54 (s, 1H), 2.52 (s, 2H), 2.22 (s, 2H), 2.03 (s, 3H), 0.94 (s, 6H). <sup>13</sup>C NMR (101 MHz, DMSO-*d*<sub>6</sub>) δ 171.93, 162.99, 119.95, 113.97, 113.18, 76.60, 45.33, 42.48, 32.49, 27.80 (2C), 25.50. HRMS: The *m/z* [M + H]<sup>+</sup> was calculated as 187.1157, and the measured value was 187.1307.

For synthesis and characterization of **LDM-OH**, a solution of compound **1** (370.40 mg, 1.98 mmol) in ethanol (25 mL) was added

4-Hydroxybenzaldehyde (318.30 mg, 2.61 mmol) and two drops of piperidine. The reaction was allowed to heat and reflux for 12 h. Purification of crude product by silica gel column chromatography to obtain red solid (531.10 mg, 91.50%). Melting point: 200.4–201.5°C; TLC (DCM/MeOH = 20:1, V/V): R<sub>f</sub> = 0.25; <sup>1</sup>H NMR (400 MHz, DMSO-*d*<sub>6</sub>) δ 10.0 (s, 1H), 7.6 (d, *J* = 8.6 Hz, 2H), 7.3–7.1 (m, 2H), 6.8 (s, 1H), 6.8 (s, 2H), 2.6 (s, 2H), 2.5 (s, 2H), 1.0 (s, 6H). <sup>13</sup>C NMR (101 MHz, DMSO) δ 170.21, 159.34, 156.65, 138.25, 129.85 (2C), 127.10, 126.22, 121.36, 115.87 (2C), 114.11, 113.29, 74.81, 42.29, 38.17, 31.63, 27.42 (2C). HRMS: The *m/z* [M + H]<sup>+</sup> was calculated as 291.1419, and the measured value was 291.1591.

For synthesis and characterization of **LDM**, a solution of **LDM-OH** (200.52 mg, 0.685 mmol) in CH<sub>2</sub>Cl<sub>2</sub> (15 mL) was added dimethylaminothioformyl chloride (126.40 mg, 1.028 mmol) and 0.92 mmol (127.13 mg) of K<sub>2</sub>CO<sub>3</sub>. The reaction was allowed to heat and reflux for 4 h. Purification of crude product by silica gel column chromatography to obtain yellow powder (176.42 mg, 68.31%). TLC (DCM/EA = 30:1, V/V): R<sub>f</sub> = 0.22; <sup>1</sup>H NMR (400 MHz, DMSO-*d*<sub>6</sub>) δ 7.73 (d, *J* = 8.5 Hz, 2H), 7.36 (m, 2H), 7.12 (d, *J* = 8.4 Hz, 2H), 6.90 (s, 1H), 3.35 (d, *J* = 19.8 Hz, 6H), 2.59 (d, *J* = 27.8 Hz, 4H), 1.03 (s, 6H). <sup>13</sup>C NMR (101 MHz, DMSO) δ 186.52, 170.81, 156.25, 155.03, 137.11, 133.99, 129.09 (2C), 123.85 (2C), 123.32, 114.32, 113.50, 76.90, 43.30, 42.78, 39.04, 38.65, 32.16, 27.92 (2C). HRMS: The *m/z* [M + H]<sup>+</sup> was calculated as 377.2741, and the measured value was 377.2653.

### Preparation of detection solution for probe **LDM**

For the preparation of probe reserve solution, first, weigh the yellow solid powder **LDM** and dissolve it in Dimethyl sulfoxide (DMSO) to obtain **LDM** stock solution (20.0 μM). Then dilute the stock solution to 10.0 μM with PBS (DMSO-PBS, pH = 7.4, 1:99, v/v), and record UV and fluorescence spectra at 37 °C.

For the preparation of analytes for selective experiments, the various anionic solutions required for the experiment (F<sup>-</sup>, HPO<sub>4</sub><sup>2-</sup>, Cl<sup>-</sup>, SO<sub>4</sub><sup>2-</sup>, PO<sub>4</sub><sup>3-</sup>, CH<sub>3</sub>COO<sup>-</sup>) come from the corresponding sodium salts; Various metal cation solutions (Cd<sup>2+</sup>, Ag<sup>+</sup>, Al<sup>3+</sup>, Ca<sup>2+</sup>, Cr<sup>3+</sup>, Co<sup>2+</sup>, Fe<sup>2+</sup>, Fe<sup>3+</sup>, Mn<sup>2+</sup>, Ni<sup>2+</sup>, Pb<sup>2+</sup>, Zn<sup>2+</sup>, Hg<sup>2+</sup> and Cu<sup>2+</sup>) are prepared from corresponding chloride salts or sulfates. These solutions have a concentration of 0.01 mol/L.

**LDM** was dissolved in PBS buffer (0.01 M, pH = 7.4) as a reserve solution (1 mM). Various reactive oxygen species (ROS) and reactive nitrogen species (RNS), including NO<sub>2</sub><sup>-</sup>, NO<sub>3</sub><sup>-</sup>, ClO<sup>-</sup>, H<sub>2</sub>O<sub>2</sub>, <sup>1</sup>O<sub>2</sub>, •OH, NO, t-BuOO<sup>-</sup>, ONOO<sup>-</sup>, and •O<sub>2</sub><sup>-</sup> were prepared using the following method. NO<sub>2</sub><sup>-</sup>, NO<sub>3</sub><sup>-</sup> and •O<sub>2</sub><sup>-</sup> were prepared with corresponding sodium salts NaNO<sub>2</sub>, NaNO<sub>3</sub> and KO<sub>2</sub>, respectively, with a final concentration of 0.01 M. The 30% H<sub>2</sub>O<sub>2</sub> solution was diluted and concentration was determined by light absorption at 240 nm (ε = 43.6 M<sup>-1</sup>cm<sup>-1</sup>). The commercially available Sodium hypochlorite solution was used as the source of Hypochlorite, and the concentration of Hypochlorite (ClO<sup>-</sup>) was determined at 292 nm using a molar absorption rate of 350 M<sup>-1</sup>cm<sup>-1</sup>. 1 mL of H<sub>2</sub>O<sub>2</sub> solution (0.1 mol/L) and 1 mL of NaClO solution (0.1 mol/L) were mixed to prepare singlet oxygen (<sup>1</sup>O<sub>2</sub>), then diluted to 10 mL. (NH<sub>4</sub>)<sub>2</sub>Fe(SO<sub>4</sub>)<sub>2</sub>·6H<sub>2</sub>O mixed with 10 equivalents of H<sub>2</sub>O<sub>2</sub> to prepare hydroxyl radicals (•OH), and the concentration of •OH was calculated based on the Fe<sup>2+</sup> concentration. Nitric oxide (NO) was produced from Nitroso iron Sodium cyanide (III). The t-BuOO<sup>-</sup> was generated by t-BuOOH. Add NaNO<sub>2</sub>, HCl, and H<sub>2</sub>O<sub>2</sub> to the NaOH solution to produce ONOO<sup>-</sup>. The concentration of ONOO<sup>-</sup> was measured at 302 nm using a molar absorption rate of 1670 M<sup>-1</sup>cm<sup>-1</sup>.

### Molecular docking

A theoretical simulation technique called molecular docking is used to analyze intermolecular interactions and forecast intermolecular binding affinities and patterns. Molecular docking was carried out with Discovery Studio to investigate the interactions between luteolin and

the proteins in the core network. First, ChemDraw software was used to draw the **LDM-OH** structure and saved it as a sdf format file. Then, 7 protein crystal structures were retrieved from the UniProt (<https://www.uniprot.org/>), dehydrated, hydrogenated, and molecular docking using Discovery Studio Tools, and saved as pdbqt files. Next, the target proteins that were also monitored in this experiment were visualized and analyzed using Discovery Studio 2019. Finally, Pymol software identified the interacting amino acids and output the image format.

### Cell culture

HepG<sub>2</sub>/HeLa cells were cultured in Dulbecco's modified Eagle's medium (VivaCell, Shanghai, China) supplemented with 10% fetal bovine serum, penicillin (100 units/ml), and streptomycin (100 µg/ml; 10,000 units/ml) in a 5% CO<sub>2</sub> humidified incubator at 37 °C. Cells were obtained from Procell Life Science&Technology Co., Ltd. (Wuhan, China).

### Cell treatment and imaging

A total of  $2 \times 10^5$  cells were seeded on a glass-bottom micro-well dish and incubated with 2 ml of DMEM supplemented with 10% FBS for 24 h, then stained with **LDM** (10 µM) or **LDM-OH** (10 µM) for 30 min, and with 100 nM Lipi-B (blue commercial LD dye, Dojindo Laboratories Kumamoto) at 37 °C for another 30 min, the cells were washed 3 times with pre-warmed free DMEM, and washed with free DMEM 3 times. Lastly, The HeLa/HepG<sub>2</sub> cells were observed under super-resolution microscope or confocal laser scanning microscopy (LSM-980, Zeiss) and analyzed with ImageJ software. In addition, *Pearson correlation coefficient* (PCC, the degree of overlap between two fluorescent channels, pixel-based) was analyzed for co-localization using ImageJ software equipped a colocalization analysis plugin as previously reported<sup>56</sup>. For more information, please refer to: <https://imagej.net/ij/plugins/colocalization-finder.html>.

### FA migration experiment

After incubating the cells in complete medium containing 1.0 µM BODIPY<sup>TM</sup> FL C12<sup>488</sup> (Thermo Fisher Scientific) for 16 h, wash the cells twice with PBS to remove excess C12<sup>488</sup>. Then, label the mitochondria/LD with MTDRLipi-B<sup>405</sup> respectively, and use confocal laser scanning microscopy for imaging. Analyze and calculate the overlap coefficient between FAs and mitochondria using ImageJ software to evaluate the migration rate of FAs from LD to mitochondria.

### Data analysis

Statistical analysis was performed with Prism 8 (GraphPad). Normality and lognormality test to check the normal distribution. In the case of normal distribution, the statistical comparison of results was tested with a *t*-test. In the case of non-normal distribution, statistical analysis was performed using two-tailed unpaired Student's *t*-test, and the data were presented as mean ± SD, *P* < 0.05 was considered statistically significant. Source data are provided as a source data file. Analyzed cells were obtained from three replicates. Statistical significance and sample sizes in all graphs are indicated in the corresponding Fig. legends.

### Reporting summary

Further information on research design is available in the Nature Portfolio Reporting Summary linked to this article.

### Data availability

All data are available from the corresponding author on request. Source data are provided with this paper. The original files of all images included in figures have been deposited in Zenodo with the identifier <https://zenodo.org/records/13938287> Source data are provided with this paper.

## References

- Grabner, G. F., Xie, H., Schweiger, M. & Zechner, R. Lipolysis: cellular mechanisms for lipid mobilization from fat stores. *Nat. Metab.* **3**, 1445–1465 (2021).
- Roberts, M. A. & Olzmann, J. A. Protein Quality Control and Lipid Droplet Metabolism. *Annu Rev. Cell Dev. Biol.* **36**, 115–139 (2020).
- Mece, O. et al. Lipid droplet degradation by autophagy connects mitochondria metabolism to Prox1-driven expression of lymphatic genes and lymphangiogenesis. *Nat. Commun.* **13**, 2760 (2022).
- Talari, N. K. et al. Lipid-droplet associated mitochondria promote fatty-acid oxidation through a distinct bioenergetic pattern in male Wistar rats. *Nat. Commun.* **14**, 766 (2023).
- Olzmann, J. A. & Carvalho, P. Dynamics and functions of lipid droplets. *Nat. Rev. Mol. Cell Biol.* **20**, 137–155 (2019).
- Mau, K. H. T. et al. Dynamic enlargement and mobilization of lipid droplets in pluripotent cells coordinate morphogenesis during mouse peri-implantation development. *Nat. Commun.* **13**, 3861 (2022).
- Tian, H. et al. Fluorescent probes for the imaging of lipid droplets in live cells. *Coordination Chemistry Reviews* **427**, <https://doi.org/10.1016/j.ccr.2020.213577> (2021).
- Chen, J. et al. Stable Super-Resolution Imaging of Lipid Droplet Dynamics through a Buffer Strategy with a Hydrogen-Bond Sensitive Fluorogenic Probe. *Angew. Chem. Int Ed. Engl.* **60**, 25104–25113 (2021).
- Liu, G. et al. Ultrabright organic fluorescent probe for quantifying the dynamics of cytosolic/nuclear lipid droplets. *Biosensors and Bioelectronics* **241**, <https://doi.org/10.1016/j.bios.2023.115707> (2023).
- Song, C. W. et al. A rationally designed polarity–viscosity sensitive probe for imaging lipid droplets. *Dyes and Pigments* **171**, <https://doi.org/10.1016/j.dyepig.2019.107718> (2019).
- Ye, Z. et al. In-Sequence High-Specificity Dual-Reporter Unlocking of Fluorescent Probe Enables the Precise Identification of Atherosclerotic Plaques. *Angew. Chem. Int Ed. Engl.* **61**, e202204518 (2022).
- Fan, L. et al. Lipid Droplet-Specific Fluorescent Probe for In Vivo Visualization of Polarity in Fatty Liver, Inflammation, and Cancer Models. *Anal. Chem.* **93**, 8019–8026 (2021).
- Halaoui, R. & McCaffrey, L. Rewiring cell polarity signaling in cancer. *Oncogene* **34**, 939–950 (2015).
- Zhanghao, K. et al. High-dimensional super-resolution imaging reveals heterogeneity and dynamics of subcellular lipid membranes. *Nat. Commun.* **11**, 5890 (2020).
- Peng, G. et al. Highly Efficient Red/NIR-Emissive Fluorescent Probe with Polarity-Sensitive Character for Visualizing Cellular Lipid Droplets and Determining Their Polarity. *Anal. Chem.* **94**, 12095–12102 (2022).
- Zhang, J. et al. Mitochondrial-Targeted Delivery of Polyphenol-Mediated Antioxidases Complexes against Pyroptosis and Inflammatory Diseases. *Adv. Mater.* **35**, e2208571 (2023).
- Li, Y. et al. Engineering polyphenols with biological functions via polyphenol-protein interactions as additives for functional foods. *Trends Food Sci. Technol.* **110**, 470–482 (2021).
- Shi, D., Liu, W., Wang, G., Guo, Y. & Li, J. Small-molecule fluorescence-based probes for aging diagnosis %J. *Acta Mater. Med.* **1**, 4–23 (2022).
- Zhang, X. et al. Ratiometric fluorescent probes for capturing endogenous hypochlorous acid in the lungs of mice. *Chem. Sci.* **9**, 8207–8212 (2018).
- Yao, L., Song, H., Yin, C. & Huo, F. An ICT-switched fluorescent probe for visualizing lipid and HClO in lipid droplets during ferroptosis. *Chem. Commun.* **60**, 835–838 (2024).
- Yang, X. et al. Visualization of biothiols and HClO in cancer therapy via a multi-responsive fluorescent probe. *Sensors and Actuators B: Chemical* **347**, <https://doi.org/10.1016/j.snb.2021.130620> (2021).

22. Lu, J. et al. Assessing Early Atherosclerosis by Detecting and Imaging of Hypochlorous Acid and Phosphorylation Using Fluorescence Nanoprobe. *Advanced Materials* **35**, <https://doi.org/10.1002/adma.202307008> (2023).
23. Zadoorian, A., Du, X. & Yang, H. Lipid droplet biogenesis and functions in health and disease. *Nat. Rev. Endocrinol.* **19**, 443–459 (2023).
24. Kitamura, T., Takagi, S., Naganuma, T. & Kihara, A. Mouse aldehyde dehydrogenase ALDH3B2 is localized to lipid droplets via two C-terminal tryptophan residues and lipid modification. *Biochem J.* **465**, 79–87 (2015).
25. Schwefel, D. et al. Structural insights into the mechanism of GTPase activation in the GIMAP family. *Structure* **21**, 550–559 (2013).
26. Cobbe, N. et al. The conserved metalloprotease invadolisin localizes to the surface of lipid droplets. *J. Cell Sci.* **122**, 3414–3423 (2009).
27. Yuan, M., Lin, X., Wang, D. & Dai, J. Proteins: Neglected active ingredients in edible bird's nest. *Chin. Herb. Med.* **15**, 383–390 (2023).
28. Zhou, R. et al. Stimulated Emission Depletion (STED) Super-Resolution Imaging with an Advanced Organic Fluorescent Probe: Visualizing the Cellular Lipid Droplets at the Unprecedented Nanoscale Resolution. *ACS Mater. Lett.* **3**, 516–524 (2021).
29. Zhou, R. et al. A new organic molecular probe as a powerful tool for fluorescence imaging and biological study of lipid droplets. *Theranostics* **13**, 95–105 (2023).
30. Cao, M. et al. Structure Rigidification Promoted Ultrabright Solvatochromic Fluorescent Probes for Super-Resolution Imaging of Cytosolic and Nuclear Lipid Droplets. *Anal. Chem.* **94**, 10676–10684 (2022).
31. Dai, J. et al. Super-resolution dynamic tracking of cellular lipid droplets employing with a photostable deep red fluorogenic probe. *Biosensors and Bioelectronics* **229**, <https://doi.org/10.1016/j.bios.2023.115243> (2023).
32. Chen, Q. et al. A dual-labeling probe to track functional mitochondria-lysosome interactions in live cells. *Nat. Commun.* **11**, 6290 (2020).
33. Wu, Y. & Shroff, H. Faster, sharper, and deeper: structured illumination microscopy for biological imaging. *Nat. Methods* **15**, 1011–1019 (2018).
34. Bickel, P. E., Tansey, J. T. & Welte, M. A. PAT proteins, an ancient family of lipid droplet proteins that regulate cellular lipid stores. *Biochimica et. Biophysica Acta (BBA) - Mol. Cell Biol. Lipids* **1791**, 419–440 (2009).
35. Wu, Y. et al. Plin2-mediated lipid droplet mobilization accelerates exit from pluripotency by lipidomic remodeling and histone acetylation. *Cell Death Differ.* **29**, 2316–2331 (2022).
36. Kong, F. et al. Traditional Chinese medicines for non-small cell lung cancer: Therapies and mechanisms. *Chin. Herb. Med.* **15**, 509–515 (2023).
37. Lyu, X. et al. A gel-like condensation of Cidec generates lipid-permeable plates for lipid droplet fusion. *Dev. Cell* **56**, 2592–2606 e2597 (2021).
38. Thiam, A. R., Farese, R. V. Jr. & Walther, T. C. The biophysics and cell biology of lipid droplets. *Nat. Rev. Mol. Cell Biol.* **14**, 775–786 (2013).
39. Tatenaka, Y. et al. Monitoring Lipid Droplet Dynamics in Living Cells by Using Fluorescent Probes. *Biochemistry* **58**, 499–503 (2019).
40. Honig, B. & Shapiro, L. Adhesion Protein Structure, Molecular Affinities, and Principles of Cell-Cell Recognition. *Cell* **181**, 520–535 (2020).
41. Zhou, Z. et al. Phosphorylation regulates the binding of autophagy receptors to FIP200 Claw domain for selective autophagy initiation. *Nat. Commun.* **12**, 1570 (2021).
42. Liu, K. & Czaja, M. J. Regulation of lipid stores and metabolism by lipophagy. *Cell Death Differ.* **20**, 3–11 (2013).
43. Nakatogawa, H. Mechanisms governing autophagosome biogenesis. *Nat. Rev. Mol. Cell Biol.* **21**, 439–458 (2020).
44. Martínez-Reyes, I. & Chandel, N. S. Cancer metabolism: looking forward. *Nat. Rev. Cancer* **21**, 669–680 (2021).
45. Fan, T. et al. Metabolomic and transcriptomic profiling of hepatocellular carcinomas in Hras12V transgenic mice. *Cancer Med.* **6**, 2370–2384 (2017).
46. Liu, R. et al. Choline kinase alpha 2 acts as a protein kinase to promote lipolysis of lipid droplets. *Mol. Cell* **81**, 2722–2735.e2729 (2021).
47. Zhou, L. et al. Coordination Among Lipid Droplets, Peroxisomes, and Mitochondria Regulates Energy Expenditure Through the CIDE-ATGL-PPAR $\alpha$  Pathway in Adipocytes. *Diabetes* **67**, 1935–1948 (2018).
48. Wang, J. et al. An ESCRT-dependent step in fatty acid transfer from lipid droplets to mitochondria through VPS13D-TSG101 interactions. *Nature Communications* **12**, <https://doi.org/10.1038/s41467-021-21525-5> (2021).
49. Yu, Z. et al. In situ visualization of the cellular uptake and sub-cellular distribution of mussel oligosaccharides. *Journal of Pharmaceutical Analysis* **14**, <https://doi.org/10.1016/j.jpha.2023.12.022> (2024).
50. Tang, Z.-H. et al. Induction of reactive oxygen species-stimulated distinctive autophagy by chelerythrine in non-small cell lung cancer cells. *Redox Biol.* **12**, 367–376 (2017).
51. Gao, W.-Y. et al. Tanshinone IIA Downregulates Lipogenic Gene Expression and Attenuates Lipid Accumulation through the Modulation of LXR $\alpha$ /SREBP1 Pathway in HepG2 Cells. *Biomedicines* **9**, <https://doi.org/10.3390/biomedicines9030326> (2021).
52. Dean, K. M. & Palmer, A. E. Advances in fluorescence labeling strategies for dynamic cellular imaging. *Nat. Chem. Biol.* **10**, 512–523 (2014).
53. Sancho, A., Vandersmissen, I., Craps, S., Lutun, A. & Groll, J. A new strategy to measure intercellular adhesion forces in mature cell-cell contacts. *Sci. Rep.* **7**, 46152 (2017).
54. Henne, W. M., Reese, M. L. & Goodman, J. M. The assembly of lipid droplets and their roles in challenged cells. *EMBO J* **37**, <https://doi.org/10.15252/emboj.201898947> (2018).
55. Ramosaj, M. et al. Lipid droplet availability affects neural stem/progenitor cell metabolism and proliferation. *Nat. Commun.* **12**, 7362 (2021).
56. Gerst, R., Cseresnyés, Z. & Figge, M. T. JIPipe: visual batch processing for ImageJ. *Nat. Methods* **20**, 168–169 (2023).

## Acknowledgements

Q.C. was funded by Young Elite Scientists Sponsorship Program by CACM (CACM-2023-QNRC1-02), Shandong Province Key R&D Program (Major Technological Innovation Project) (2021CXGC010501), National Natural Science Foundation of China (Nos. 22107059), Natural Science Foundation of Shandong Province (ZR2021QH057), Innovation Team of Shandong Higher School Youth Innovation Technology Program (2021KJ035), Taishan Scholars Program (TSQN202211221), Shandong Science Fund for Excellent Young Scholars (ZR2022YQ66), and Joint Innovation Team for Clinical & Basic Research (202408); X.C. was funded by National University of Singapore (NUHSRO/2020/133/Startup/08, NUHSRO/2023/008/NUSMed/TCE/LOA, NUHSRO/2021/034/TRP/09/Nanomedicine, NUHSRO/2021/044/Kickstart/09/LOA, 23-0173-A0001), National Medical Research Council (MOH-001388-00, CG21AP1005, MOH-001500-00, MOH-001609-00), Singapore Ministry of Education (MOE-000387-00), and National Research Foundation (NRF-000352-00).

## Author contributions

L.K., Q.B. and Q.W. collected all 3D-SIM super-resolution microscopy data. L.K., Q.B. and C.L. analyzed and processed the SIM data. X.S. cultured cell. L.K., C.W. (Yongchun Wei) and F.W. (Yanfeng Wang) synthesized and B.S. characterized LDM. J.S., Z.Y., and J.Y. performed confocal laser scanning microscopy. L.K. and H.F. performed Molecular docking data. X.C. and Q.C. conceived the project, designed

the experiments, and wrote the manuscript with the help of all authors.

### Competing interests

The authors declare no competing interests.

### Additional information

**Supplementary information** The online version contains supplementary material available at <https://doi.org/10.1038/s41467-024-53667-7>.

**Correspondence** and requests for materials should be addressed to Xiaoyuan Chen or Qixin Chen.

**Peer review information** *Nature Communications* thanks Chuan Dong, Zhaochao Xu and the other, anonymous, reviewer(s) for their contribution to the peer review of this work. A peer review file is available.

**Reprints and permissions information** is available at <http://www.nature.com/reprints>

**Publisher's note** Springer Nature remains neutral with regard to jurisdictional claims in published maps and institutional affiliations.

**Open Access** This article is licensed under a Creative Commons Attribution-NonCommercial-NoDerivatives 4.0 International License, which permits any non-commercial use, sharing, distribution and reproduction in any medium or format, as long as you give appropriate credit to the original author(s) and the source, provide a link to the Creative Commons licence, and indicate if you modified the licensed material. You do not have permission under this licence to share adapted material derived from this article or parts of it. The images or other third party material in this article are included in the article's Creative Commons licence, unless indicated otherwise in a credit line to the material. If material is not included in the article's Creative Commons licence and your intended use is not permitted by statutory regulation or exceeds the permitted use, you will need to obtain permission directly from the copyright holder. To view a copy of this licence, visit <http://creativecommons.org/licenses/by-nc-nd/4.0/>.

© The Author(s) 2024